Combustion and Flame 260 (2024) 113220

Contents lists available at ScienceDirect

Combustion and Flame

journal homepage: www.sciencedirect.com/journal/combustion-and-flame

Experimental and numerical investigation on soot formation and evolution of particle size distribution in laminar counterflow ethylene flames

Abhijit Kalbhor [a,*], Robert Schmitz [b,1], Astrid Ramirez [c,g], Petros Vlavakis [d], Fabian P. Hagen [d], Federica Ferraro [b], Marina Braun-Unkhoff [c,g], Trupti Kathrotia [g], Uwe Riedel [f], Dimosthenis Trimis [d], Jeroen van Oijen [a], Christian Hasse [b], Daniel Mira [e]

[a] Eindhoven University of Technology, Eindhoven, The Netherlands
[b] Technical University of Darmstadt, Department of Mechanical Engineering, Simulation of reactive Thermo-Fluid Systems, Otto-Berndt-Str. 2, 64287 Darmstadt, Germany
[c] University of Stuttgart, Stuttgart, Germany
[d] Karlsruhe Institute of Technology (KIT), Karlsruhe, Germany
[e] Barcelona Supercomputing Centre, Barcelona, Spain
[f] German Aerospace Center, Cottbus, Germany
[g] German Aerospace Center, Stuttgart, Germany

ARTICLE INFO

Keywords:
Soot formation
Counterflow non-premixed flames
Discrete sectional method
Split-based extended quadrature method of moments
Particle size distribution

ABSTRACT

A detailed investigation of the process of soot formation in ethylene-fueled laminar counterflow diffusion flames is conducted using dedicated experiments and numerical simulations. Two different strategies based on the Discrete Sectional Method (DSM) and the Split-based Quadrature Method of Moments (S-EQMOM) are considered to model the evolution of soot particle size distributions, and their comparative assessment is carried out for soot formation prediction and particle growth. A consistent chemical reaction mechanism describing the oxidation of hydrocarbon fuels and the prediction of soot precursors with the growth of polycyclic aromatic hydrocarbons (PAHs) up to pyrene ($C_{16}H_{10}$) is examined. Experiments for various strain rates and fuel compositions are performed to assess the sensitivity of soot production to these two parameters. The results show that both modeling strategies captured well the qualitative trends of soot volume fraction under variations in strain rate and mixture composition, with slight over-prediction of the peak values. For both soot models, a higher sensitivity of soot formation is noticed by changes in mixture composition compared to those of strain rate variation. Additionally, the soot models demonstrated promising performance in capturing the experimentally observed evolution of the soot particle size distribution (PSD).

1. Introduction

The emission of particulate matter (predominantly soot) from combustion systems is one of the major concerns due to its harmful effects on human health and the environment. Soot particles can range from large sizes that tend to precipitate by gravity, to small sizes that remain in the atmosphere causing more adverse issues such as respiratory problems. Especially soot particles emitted by aero-engines, typically in higher altitudes, absorb sunlight and affect cloud formation when acting as condensation nuclei leading to contrails [1]. For all these reasons, current emission regulations in both air and road transportation are targeting not only soot volume fraction but also particle size distributions [2]. The present-day emission legislation is based on integral values such as soot particle number density or soot particle mass concentration. In fact, the physical and chemical processes associated with soot formation depend on the size distribution of the particles themselves, especially, soot oxidation, which significantly influences the final particle concentrations during subsequent processes in non-premixed flames [3,4]. Therefore, incorporating the size distribution in addition to integral quantities, such as soot volume fraction, is of significant interest to further understand the soot formation process and develop appropriate models for predicting their characteristics.

Soot chemistry is characterized by slower time scales than that of fuel oxidation [5,6]. Therefore, soot formation may be appreciably influenced by characteristics of flow time scales that alter the residence time of particles in a flame [7]. In practical combustion devices, which often operate under turbulent conditions, the soot formation

* Corresponding author.
E-mail address: a.j.kalbhor@tue.nl (A. Kalbhor).
[1] Joint First Authors.

https://doi.org/10.1016/j.combustflame.2023.113220
Received 3 April 2023; Received in revised form 13 November 2023; Accepted 24 November 2023

process is highly affected by complex interactions of reactive flow, flame, and soot. Therefore, understanding soot response to flow variations is an important research topic concerning predictive soot model development.

In this context, the counterflow diffusion flame is an attractive configuration for systematic studies analyzing flow time effects on soot formation through strain rate variations. Several experimental [8–12] and numerical investigations [11–13] have addressed soot sensitivity to strain rate for different fuels in counterflow configurations. It is shown that increased strain rates inhibit soot formation (indicated by soot volume fraction and PAH concentrations, e.g., pyrene concentration) as a consequence of the lower residence times. While these studies have contributed to understanding physical and chemical mechanisms associated with interactions between flow and soot in more detail, the systematic investigation of strain rate effects on the evolution of soot particle size distribution in a counterflow configuration remains limited. In addition, this configuration is suitable to investigate the sooting tendencies of different fuels in the form of a limit curve [14], as fuel composition can be manipulated with the dilution of non-hydrocarbon gases such as nitrogen. Fuel dilution with nitrogen has been shown to affect the sooting tendency through variation mainly of the flame temperature or the concentration of soot precursors [15–17].

For these reasons, we perform numerical simulations with two different state-of-the-art soot modeling strategies from recently measured counterflow flames [18] to investigate their sooting characteristics. These modeling approaches include the discrete sectional method (DSM) [19] and the split-based extended quadrature method of moments (S-EQMOM) [20], which provide direct information on the soot particle size distribution (PSD). Sets of different mixture compositions and strain rate variations are investigated with lightly and moderately sooting conditions which extends the data pool for this configuration with systematic parameter variations. The present study uniquely features detailed measurements of the soot formation by including soot volume fraction and PSD in combination with the comparison of two different soot models. Furthermore, a new comprehensive chemical kinetic mechanism referred to as ESTiMatE-Mech [21] (abbreviated name as EST3) is introduced for modeling the PAH formation chemistry. This mechanism was developed with a focus on the prediction of the PAH formation during the combustion of ethylene and a wide range of jet fuel surrogates.

Considering the rich experimental database and the different modeling approaches, the objectives of the present study are: (1) to systematically investigate the strain rate sensitivity of soot formation and the effects of fuel dilution in laminar ethylene counterflow flames by using new experiments and computations; (2) to study the evolution of soot particle size distribution under strain rate variation and fuel dilution; (3) to introduce a new chemical kinetic mechanism and validate its performance for soot prediction in laminar ethylene counterflow flames; and (4) to perform a comparative assessment of the predictive capabilities of two soot modeling strategies concerning soot formation characteristics.

The manuscript is organized as follows: the experimental setup and measurement techniques for the species, temperature, and soot quantities are described. Subsequently, the modeling study is presented in two parts. First, the kinetic mechanism is presented including validation with species and temperature profiles measured within the counterflow flames using ethylene as a fuel. Second, the performance of the two soot models in the soot prediction in counterflow flames from Wang and Chung [11] is evaluated by comparing the new reaction mechanism EST3 with the well-established KM2 mechanism [22]. The main investigation is performed on a series of ethylene counterflow diffusion flames with varying strain rates and fuel compositions [23]. The experimental data sets for soot formation and PSD evolution are compared against the simulation results. A detailed analysis of the soot formation sub-processes is provided by comparing the numerical results for both soot models. Finally, the concluding remarks and perspectives are given.

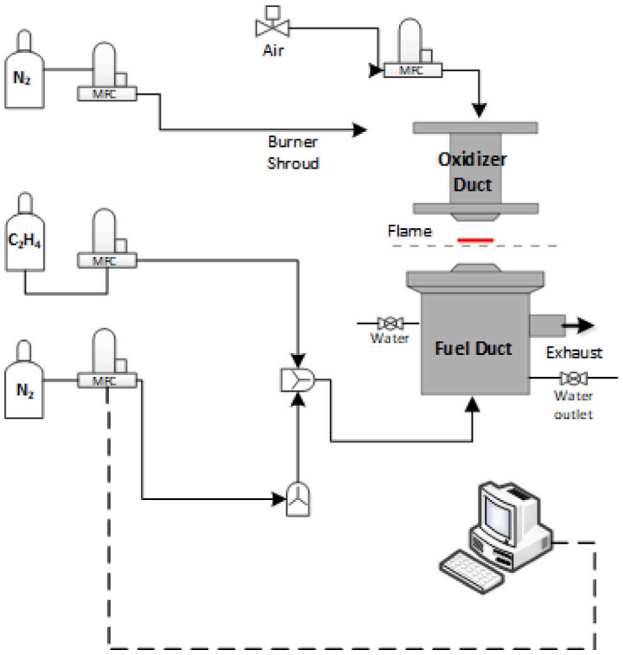

Fig. 1. Schematic of the counterflow burner.

2. Experimental approach

The counterflow setup employed in the present work is based on the burner design described in [24,25]. The details of the experimental setup consisting of intrusive particle sampling coupled with differential mobility particle sizing, i.e., a scanning mobility particle sizer (SMPS), two-color time-resolved laser-induced incandescence (2C-TiRe-LII), and fuel/oxidizer flow control systems can be found in the work of Hagen et al. [18,23]. The burner consists of two concentrically placed identical ducts with inner diameters of 25 mm, configured as opposed to each other, with a separation distance of 12.5 mm. The bottom duct (fuel duct) is surrounded by two concentric annular ducts. Nitrogen gas shielding is applied through the inner annular gap to avoid ambient air interference and the formation of secondary edge flames. To facilitate the suction of product gases, an outermost annular duct is connected to an exhaust system. Similar to the fuel duct, the oxidizer duct is also shrouded by nitrogen. To ensure plug-flow type boundary conditions, multiple stainless steel wire screens (200 meshes/inch) are placed at the nozzle exit. The flow rates are adjusted by thermal mass flow controllers (MFC) with an uncertainty of less than 1%. The schematic of the counterflow burner setup is shown in Fig. 1.

In the present experiments, ethylene with a purity of > 99.9% is used as fuel diluted with nitrogen, while synthetic air (21% O_2/79% N_2 by volume) is used as an oxidizer. For the shielding and dilution of the fuel, nitrogen with a purity of > 99.999% is used. The fuel and oxidizer are maintained at 300 K ambient temperature under atmospheric pressure. In the experiments, a momentum balance is imposed to ensure the stagnation plane formed by the reactant streams lies approximately in the central region between the two ducts. In the counterflow burner, the global strain rate of the oxidizer is defined as:

$$K = \frac{2|u_o|}{L}\left(1 + \frac{|u_f|\sqrt{\rho_f}}{|u_o|\sqrt{\rho_o}}\right), \tag{1}$$

where u denotes the flow velocity of reactants, L represents nozzle separation distance, and ρ is the gas density. Subscripts f and o indicate the fuel and oxidizer streams, respectively. Under the momentum balance ($\rho_f u_f^2 = \rho_o u_o^2$), global strain rate simplifies to $K = 4u_o/L$. In the current study, variation in global strain rate and stoichiometric

Table 1
Strain rates and fuel compositions of the investigated ethylene-air counterflow flames.

Flame	C_2H_4 mass fraction in fuel ($Y_{F,f}$) [–]	Strain rate (K) [s^{-1}]
1	0.20	60
2	0.25	60
3	0.30	50
4	0.30	60
5	0.30	70
6	0.35	60
7	0.25	100

mixture composition is achieved by altering the nozzle exit velocities of reactants and the mass fraction of ethylene in the fuel stream ($Y_{F,f}$). The experimental conditions of the investigated flames are summarized in Table 1.

In this study, temperature, concentrations of gaseous species, soot volume fractions f_v and mobility particle size distributions $P(d_m)$ are measured along the flame axis to obtain the profiles as a function of the height above the fuel duct (HAB for brevity). Temperatures were determined using a 300 μm wire diameter (after coating) S-type thermocouple that was built in-house and is described in detail in [25]. Taking into account the standard deviation of the measurement and the uncertainties imposed by the radiation correction [26], the highest level of uncertainty of the reported temperatures is 80 K [18,25]. The influence of soot deposits on radiation correction can be neglected since the residence time of the thermocouple in the low-sooting counterflow flames was chosen to be less than three seconds.

Gas chromatography coupled with mass spectrometry (GC/MS) is used to quantify gas species concentrations in the examined flames via probing gas phase species. The used sampling system consisting of a chemically inert, deactivated aluminum oxide (Al_2O_3) tube (ID 0.3 mm/OD 0.5 mm, 25 mm length) is explained in [24,25]. This micro-probe is connected to a 1/16″ stainless steel tube, which in turn is fixed through a reducer fitting to a 6 mm stainless steel tube. The transfer line connecting the flame probe to the gas GC/MS is heated up to 423 K in order to prevent condensation of species from the flame probe. The GC/MS is equipped with a Thermal Conductivity Detector (TCD) for quantifying permanent gases (CO, CO_2, O_2, H_2O, and H_2) and two Flame Ionization Detectors (FID) for hydrocarbons. Details of the GC/MS, the probe as well as the sampling system used for these investigations are given in the work from Sentko et al. [27].

The GC/MS was calibrated with gaseous and liquid mixtures. Gas calibration of the GC/MS is performed with calibration reference gas mixtures consisting of CO, CO_2, O_2, H_2, N_2, CH_4, C_2H_2, and C_6H_6. On the other hand, higher hydrocarbons and PAHs were calibrated with liquid reference mixtures fed to the GC/MS using a calibration unit consisting of a syringe pump and a direct vaporizer, or by liquid injection. Both methods showed excellent agreement and were used for different concentration levels. To ensure accurate quantification, all species subjected to quantitative analysis were calibrated at least at two different concentration levels, i.e., in a two-point calibration. The overall uncertainty on the reported concentrations is ± 3%–10% for the major species (N_2, O_2, H_2, CO, CO_2, and CH_4), ± 5%–30% for light and heavy hydrocarbons, which include several soot precursors (i.e., styrene, ethylbenzene, naphthalene, pyrene, etc.), and ± 20% for water. These values correspond to the largest uncertainty of the species in the flames studied, taking into account the standard deviations of three repeated measurements and the uncertainties from the calibration procedures. The latter includes the uncertainties in concentrations of reference gases and liquids. Note that there is an additional error in the measured mole fractions arising from the non-isokinetic sampling, which has already been discussed in [28]. The limit of detection (LOD) for the higher PAHs, i.e., the three- and four-ring systems, is 1 ppm.

For the measurement of volume fraction f_v and mobility size distribution $P(d_m)$ of soot particles formed in the investigated counterflow flames, a particle sampling system coupled with differential mobility particle sizing, i.e. SMPS, described in detail in [23], is employed. Aerosol sampling features a tailored probe that is traversed through the flame in combination with a two-stage dilution system. The dual-port probe consists of a double-walled quartz tube with a wall thickness of 1.0 mm, an inner diameter of 6.0 mm for the outer tube, and 3.0 mm for the inner tube, respectively. The outer tube narrows down to an inner diameter at the tip of 0.2 mm to reduce flow perturbance and minimize heat losses from the flame. The extracted aerosol sample is rapidly diluted with nitrogen in two stages to prevent further surface growth, coagulation, and oxidation processes of the particles. The resulting dilution ratio (DR) of the particle-laden flame gas sample was $DR \approx 2 \times 10^3$ [23], which simultaneously corresponds to the maximum values of [29]. To demonstrate the performance of the particle sampling system, f_v and $P(d_m)$ derived via differential mobility sizing were compared in [23] with those obtained by non-intrusive laser-based diagnostics, i.e. 2C-TiRe-LII. Thereby, excellent agreement was found. Further, a threshold for the developed probe was discussed, beyond which no influence of DR on $P(d_m)$ and f_v was observed. In this study, the dilution ratio DR exceeded this threshold. A sketch of the aerosol probe and a description of the methods used to determine and control DR is given in [23]. The approach for correcting $P(d_m)$ for particle losses in the probe and tubes is also provided in [23]. For differential mobility sizing, an electrostatic classifier (EC), a soft X-ray neutralizer, a nano-differential mobility analyzer (nano-DMA), and a condensation particle counter (CPC) have been used. Details of the instrumentation can be found in [30]. As reported in [23,31], uncertainties in the dilution ratio, perturbations of the flame, sampling from a volume rather than a point source, and particle deposition in the probe lead to unavoidable uncertainties in the measurement of f_v and $P(d_m)$ of ±30%.

3. Gas-phase modeling

Complementary to the experimental study, numerical simulations of the measured ethylene flames are performed to compare the ability of the models to predict the main features of the flame and their sooting characteristics. The modeling assessment of the two-phase flow (solid-gas) can be divided into two main parts: gas-phase validation and soot prediction. In this section, the reaction mechanism used to describe the chemistry of the gas phase is introduced, and numerical simulations with detailed chemistry (without soot) are conducted to validate the chemical kinetic mechanism. Dedicated experiments for non-sooting conditions are used to examine the accuracy of the new reaction mechanism EST3 to reproduce the concentrations of major species and PAHs prior to the sooting flame calculations. The description of the gas-phase reaction kinetic approach, along with its validation based on experimental species and temperature data, is detailed below.

3.1. Chemical-kinetic reaction mechanism for soot formation

The chemical-kinetic reaction mechanism EST3 [21,32] is used to describe the chemical breakdown and oxidation of the ethylene fuel. In addition to the kinetics of ethylene, the EST3 mechanism was developed to model the combustion of different compositions of jet fuel surrogates as well as their components [21]. For modeling surrogates of complex practical fuels, EST3 can handle several different *iso*-alkanes up to *iso*-octane, *n*-alkanes up to *n*-dodecane, and *cyclo*-alkanes up to *cyclo*-hexane. Moreover, EST3 includes the kinetics of different potential candidates to represent the aromatics in a jet fuel surrogate formulation, such as toluene, *n*-propylbenzene, *m*-xylene, and 1,3,5-trimethylbenzene. The EST3 mechanism has been developed with a focus on the formation of PAHs up to pyrene (A4), which is considered the key precursor for soot nucleation within the employed soot models. The EST3 mechanism consists of 214 chemical species and 1539 elementary reactions.

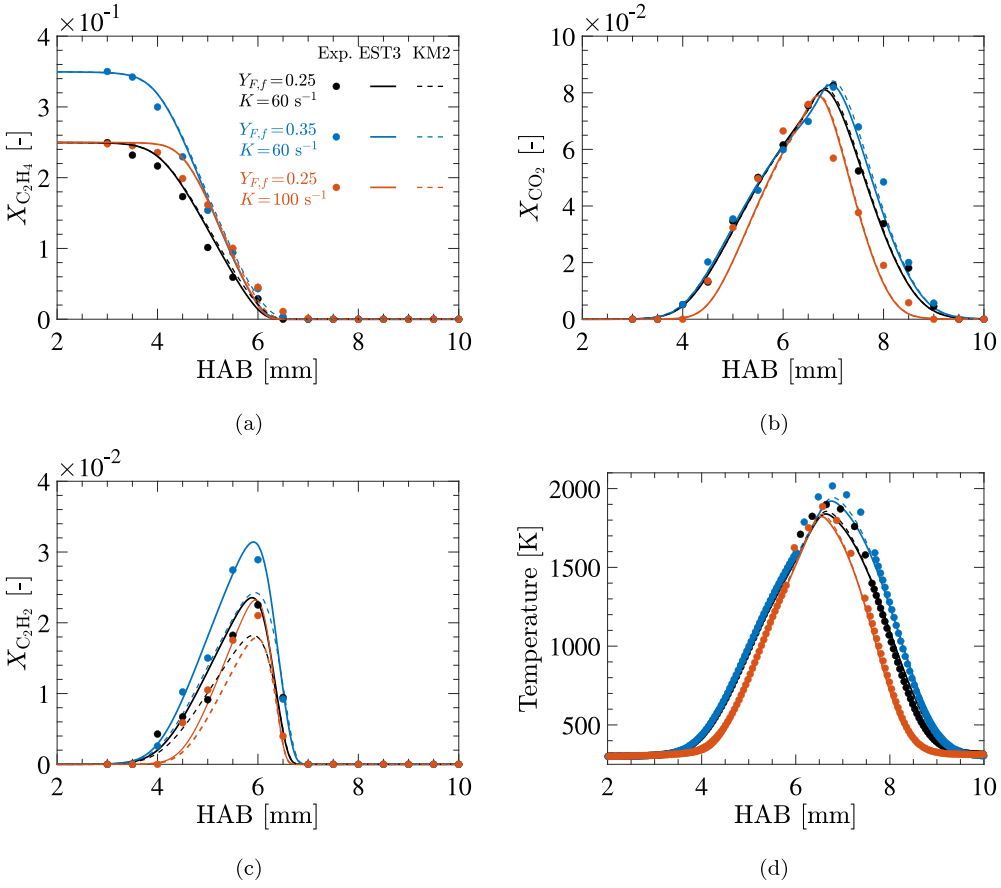

Fig. 2. Comparison between experimental (symbols) and modeling results (curves) obtained with EST3 [21,32] (solid) and KM2 [22] (dashed) mechanisms for C_2H_4, CO_2, and C_2H_2 mole fractions and temperature profiles in counterflow ethylene flames 2, 6, and 7.

In the development of EST3, a recently updated and extensively validated reaction mechanism for kerosene surrogate was selected as a base mechanism, the DLR Concise [33,34]. DLR Concise is a compact modular mechanism that encompasses the kinetics of many *n*-paraffins, *iso*-paraffins, *cyclo*-paraffins, and aromatics. To generate EST3, species that were not considered molecules of interest to be part of jet fuel surrogates were removed from the base mechanism (e.g. larger *iso*-paraffins iC > 8 and larger *n*-alkanes nC > 12). In addition, chemical kinetic sub-models of species of interest that were not yet considered in DLR Concise were developed and incorporated, such as *m*-xylene and 1,3,5-trimethylbenzene [21].

Furthermore, the chemical mechanism was updated taking into account a new detailed experimental database obtained from a counterflow burner [32]. In this counterflow burner, different fuels such as *iso*-octane, 1,3,5-trimethylbenzene, a jet A-1 surrogate, and ethylene were evaluated. This new experimental database allowed for validating and refining the mechanism, taking into account different fuels, strain rates, and fuel mass fractions. A description of the kinetics of these fuel components is omitted here for brevity; for more information, see Ref. [32]. To assure good predictability of species profiles of various PAHs within the combustion of a wide range of fuel components, some modifications based on reaction pathway (ROP) and sensitivity analysis were made, including analyses of the base mechanism [21]. Therefore, EST3 offers the capability to analyze a wide range of hydrocarbons, from lighter compounds such as ethylene to the kinetics of kerosene surrogates. It allows for consistent modeling of PAH formation that aligns well with the applied soot model. This enables efficient studies on soot formation across a diverse range of hydrocarbon fuels, including ethylene.

3.1.1. Validation of the chemical-kinetic reaction mechanism EST3

The proposed chemical-kinetic reaction mechanism of ethylene is validated for multiple PAH species including benzene (A1), toluene ($A1CH_3$), styrene (C_8H_8), indene (C_9H_8), naphthalene (A2), and acenaphthylene (A2R5). Experimental data for larger PAHs, such as phenanthrene (A3) and pyrene (A4), were unavailable as their concentrations were below their detection limits. In Fig. 2, the modeling results obtained with the EST3 mechanism are compared against the measurements for three counterflow ethylene flames with different strain rates and fuel compositions. The counterflow burner was modeled with Cantera [35] to solve the governing equations of the 1-D flame. The species diffusive mass fluxes were computed according to the multi-component formulation. The simulations are carried out for gas-phase description without the coupling of any soot model.

The spatial profiles for temperature and concentration (in mole fraction X) of major species (C_2H_4, CO_2, and C_2H_2) are shown in Fig. 2. The results from the reference mechanism, KM2 [22], are also included for completeness. As observed in Fig. 2, the profiles of major species and temperature are well captured by the EST3 mechanism. Especially, the concentration of C_2H_2, a key precursor species in soot formation, is well predicted by EST3 as compared to KM2. Besides major species, modeling results for the aromatics, such as benzene (A1), toluene ($A1CH_3$), naphthalene (A2), and pyrene (A4) are also presented in Fig. 3. The EST3 model reveals a good qualitative and quantitative predictability of benzene and naphthalene. Especially for flames with lower dilution levels, EST3 mechanism shows better quantitative prediction of toluene (Fig. 3(b)) and A2 (Fig. 3(c)) species. It is important to note that, as introduced above, the EST3 mechanism is designed to be applicable to a wide range of hydrocarbon fuels, not limited to C_1–C_4 fuels like the KM2 mechanism. However, there might be limitations in

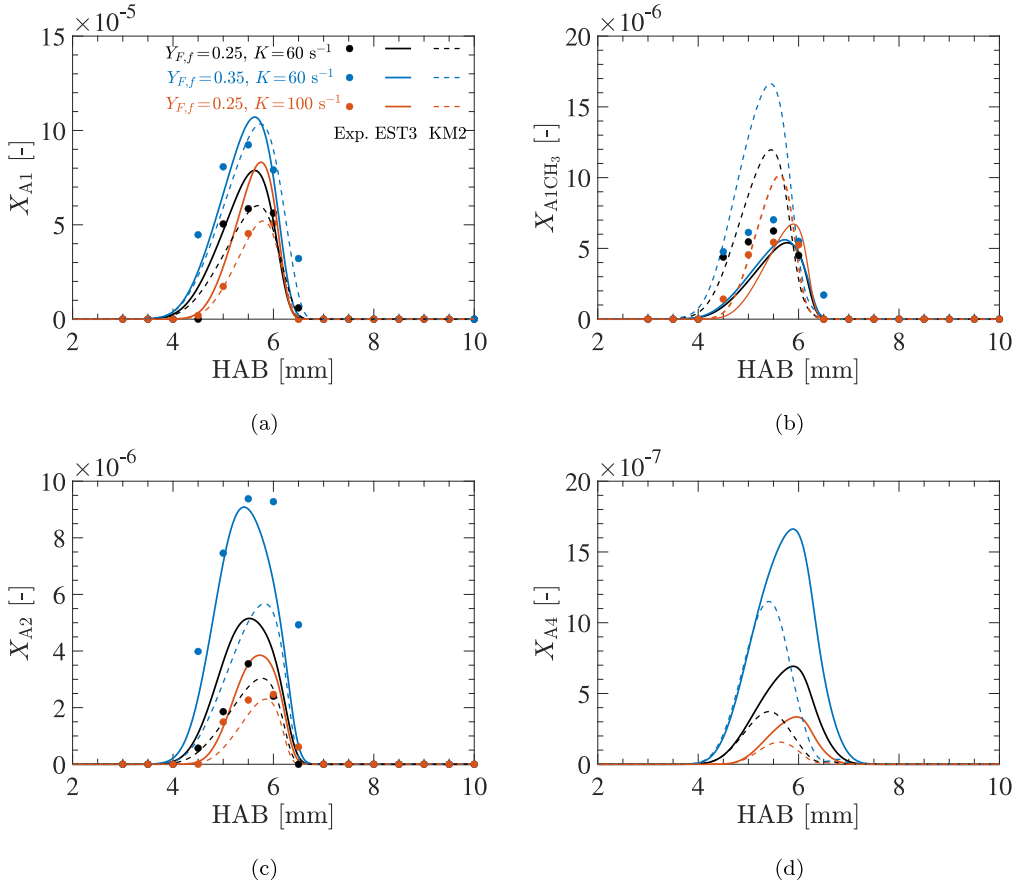

Fig. 3. Comparison between experimental (symbols) and modeling results (curves) obtained with EST3 [21,32] (solid) and KM2 [22] (dashed) mechanisms for benzene (A1), toluene ($A1CH_3$), naphthalene (A2), and pyrene (A4) mole fraction profiles in counterflow ethylene flames 2, 6, and 7.

accurately predicting each gas-phase species under certain conditions. For instance, for higher dilution and higher strain rates, these aromatic species by EST3 mechanism are overpredicted, compared to KM2.

The computed profiles of A4 are also included in Fig. 3 for analysis. However, no experimental data were available for pyrene (A4) since its concentration fell below the detection limits in this set of experiments. Compared to KM2, a higher A4 concentration is obtained with the EST3 mechanism, with a wider spatial distribution and shifted peak locations. This difference follows the expected trends since the reaction network of A4 is formulated in a way that it includes also one of all larger PAHs in the EST3 mechanism. Considering the model uncertainties associated with the reaction rate expressions for aromatic species, the predictive capabilities of the EST3 mechanism are promising. For the rest of the sections, EST3 is selected for numerical simulations.

4. Soot modeling approach

In this section, the soot formation and the evolution of particle size distribution are described using two soot models that rely on a moment-based and on a discrete representation of the population balance equations, respectively. Both models applied in this study describe a univariate evolution of the soot particles and mainly differ in the representation and approximation of the particle number density function (NDF). These models are based on the discrete sectional method (DSM) [19] and the split-based extended quadrature method of moments (S-EQMOM) [20] for describing the soot particle dynamics. The modeling approaches assume purely spherical soot particles, neglecting aggregation processes. However, the flames considered in this study are predominantly lightly to moderately sooting, hence with low levels of chain-like soot aggregates, which justifies this assumption.

4.1. Discrete sectional method (DSM)

In DSM, soot particle volume ranges are divided into a finite number of sections (using a geometric progression here). For each section, i, the governing equation for the soot mass fraction $Y_{s,i}$ is solved by taking into account flow convection, diffusion (for numerical stability), thermophoresis, and soot formation rates. The sectional soot transport equation can be formulated along the flame-normal coordinate x using a quasi-1D approximation and is given by Eq. (2):

$$\frac{\partial(\rho Y_{s,i})}{\partial t} + \frac{\partial}{\partial x}\left(\rho\left[u+v_T\right]Y_{s,i}\right) = \frac{\partial}{\partial x}\left(\rho D_{s,i}\frac{\partial Y_{s,i}}{\partial x}\right) + \rho_s \dot{Q}_{s,i}, \quad \forall\, i \in \left[1, N_{sec}\right] \tag{2}$$

where ρ_s is the density of soot particles (assumed to be 1860 kg/m^3 [19]). In the transport equation, $\dot{Q}_{s,i}$ is the sectional soot source term, and v_T is the thermophoretic velocity given by Friendlander et al. [36] as:

$$v_T = -0.55\frac{\nu}{T}\frac{\partial T}{\partial x}, \tag{3}$$

where ν is the kinematic viscosity and T is the local temperature. The diffusion coefficient of soot particles of class i is given by $D_{s,i}$. The sectional source terms $\dot{Q}_{s,i}$ include the contributions from the chemical and physical processes associated with the soot formation such as nucleation, condensation, surface growth, soot oxidation, and particle–particle coagulation.

The nucleation process is modeled through PAH (pyrene molecules here) dimerization. The reaction networks of the larger species are lumped within the gas-phase kinetics, resulting in pyrene serving as the sole surrogate species in the transition pathway from gas-phase to

young soot particles. The PAH condensation is considered as the coalescence of a PAH molecule at a soot particle surface. The growth and oxidation of soot particles by surface reactions are represented through the hydrogen-abstraction-C_2H_2-addition (HACA) mechanism [37] with rate coefficients given by Appel et al. [38]. In the surface growth model, the fraction of sites available for hydrogen abstraction is assumed to be a function of the thermal age, and particle size history [38]. The soot oxidation is considered through surface reactions involving O_2 and OH molecules with soot. The coagulation of soot particles is described following the model proposed by Kumar and Ramkrishna [39]. The morphological description of particles is not considered for simplicity. The DSM model has been validated for soot prediction in laminar flames in earlier works [19,40,41]. A detailed description of the soot model used in this study can be found in Hoerlle and Pereira [19].

4.2. Split-based extended quadrature method of moments (S-EQMOM)

In S-EQMOM [20], the number density function of the particles is approximated by its statistical properties and their moments, so it does not solve for the distribution of the particles directly. The univariate particle distribution is described using the volume V of the particles leading to the definition of the moment m_k of order k as:

$$m_k = \int_{V=V_{\min}}^{\infty} V^k n(t,x;V)\mathrm{d}V. \tag{4}$$

Herein, $n(t,x;V)$ defines the NDF of particles in space x and time t. Transport equations given in Eq. (5) for the low-order moments are considered including thermophoresis effects on soot:

$$\frac{\partial m_k}{\partial t} + \frac{\partial}{\partial x}\left(\left[u + v_T\right]m_k\right) = \dot{m}_k \tag{5}$$

The term $\dot{m}_k$ represents the sum of source terms arising due to physical and chemical soot processes such as nucleation, surface growth by the HACA-mechanism or PAH adsorption, coagulation, and oxidation analogously to the ones described in Section 4.1 for DSM. Following the approach of the Extended Quadrature Method of Moments of Yuan et al. [42], kernel density functions (KDF) of a known shape are used to approximate the PSD and therefore, enable a closure for the calculation of the moment source terms based on the distribution itself.

While in the standard EQMOM, the NDF is calculated based on the sum of the kernel density functions, and the inversion process is performed for the entire NDF, S-EQMOM splits this inversion procedure up for every sub-NDF [20]. In S-EQMOM, the moments of several coupled sub-NDFs are treated individually before the entire NDF is composed again by the sum of all sub-NDFs. This method results in an individual moment inversion step for every sub-NDF leading to a unique solution for every sub-NDF, enhanced robustness, and more stability of the inversion algorithm. The NDF $n(V)$ as the sum of individual sub-NDFs n_{s_i} is defined as:

$$n(V) = \sum_{j=1}^{N_s} n_{s_i}(V) \approx \sum_{j=1}^{N_s} w_{s_i}\delta_{\sigma_{s_i}}(V, V_{s_i}). \tag{6}$$

The sub-NDFs $n_{s_i}(V)$ in Eq. (6) are approximated by the sum of weighted sub-NDFs $\delta_{\sigma_{s_i}}$ of a defined shape following the work of Salenbauch et al. [20]. In the current study, the entire NDF is approximated with three sub-NDFs each with a gamma function shape. The individual shape parameters σ_{s_i}, weights w_{s_i}, and node positions V_{s_i} of the three applied sub-NDFs can be obtained based on the three lower-order moments of each sub-NDF. This leads to nine transported moments for reconstructing the entire particle NDF through superposition. In contrast, moments of the entire NDF get transported in the standard EQMOM. An extensive evaluation of the required number of sub-NDFs and the impact of different shapes for the sub-NDFs is provided in [20, 43]. The modeling performance of S-EQMOM has been demonstrated for premixed flames [20] and turbulent jet flames [44].

In both DSM and S-EQMOM modeling frameworks, a two-way coupling between soot chemistry and gas-phase chemistry is incorporated into the conservation equations to ensure mass/energy balance. The solvers and soot models used in this study have been rigorously verified and validated in prior research [19,20,43].

5. Assessment of the combined kinetic and soot modeling approaches

Before addressing the sooting flames from the experimental setup, we assess the combination of the kinetic scheme EST3 and the corresponding coupling with the different soot modeling strategies. This step is crucial since the soot precursor formation depends on the underlying gas-phase chemistry, and therefore subsequent soot formation results strongly depend on the used gas-phase kinetics as demonstrated in [45]. Details of the validation of the individual soot models are provided for the DSM in [19,40] and for the S-EQMOM in [20,43].

For this assessment, the counterflow ethylene flames under different strain rates, studied by Wang and Chung [11] (referred to as KAUST flames), are considered. In these flames, the fuel is C_2H_4 and the oxidizer is composed of 25% of O_2 and 75% of N_2 (on a molar basis). The reactant streams are separated with a distance of 8 mm. The flow velocities for both the fuel and oxidizer streams are varied from 15 cm/s to 30 cm/s corresponding to four global strain rates K (75 s^{-1}, 100 s^{-1}, 125 s^{-1}, and 150 s^{-1}). Simulations of counterflow flames are conducted using a steady, 1-D formulation of reacting flow equations with plug-flow type boundary conditions for the inlet streams. The 1-D laminar flamelet solvers CHEM1D [46,47] and Universal Laminar Flame solver (ULF) [48] are used for computing sooting flames with DSM and S-EQMOM models, respectively. The investigated flames are SF (soot formation) type flames, in which the flame (or reacting layer) resides on the oxidizer side of the stagnation plane. Therefore, soot particles, nucleated on the fuel-rich side of the flame, are convected away from the flame towards the stagnation plane.

Computed profiles of soot volume fraction with the DSM and S-EQMOM soot models are compared against the experimental data for different strain rates in Fig. 4. In DSM, the soot volume fraction is obtained by multiplying the total soot mass fraction with the ratio of gas and soot density, assuming a constant soot density. On the other hand, in S-EQMOM, the soot volume fraction is determined using the first moment of the Number Density Function (NDF). Simulations are performed using the EST3 kinetic mechanism introduced earlier. In addition, modeling results for the KM2 mechanism [22] are added for comparison. As it can be observed, both DSM and S-EQMOM soot modeling strategies capture the spatial distribution and the lowered peak f_v values against strain rate reasonably well. Consistent with the experimental observations, numerical profiles show that the sooting zone thickness decreases with increasing strain rates. The measured soot volume fraction is underestimated in simulations for both models, DSM and S-EQMOM, and the disparity between numerical and experimental values decreases with the strain rate. Compared to the DSM method, S-EQMOM predicts a wider sooting zone starting closer to the flame front which is in good agreement with experimental observations. On the other hand, compared to S-EQMOM, the skewness of the f_v distribution is better reproduced by DSM. At the particle stagnation position, the diffusion transport and source term for soot balance leads to a sharp decrement in f_v, which is consistent with the experimentally observed leakage of soot through the stagnation plane. Both DSM and S-EQMOM strategies favorably predict the strain rate influence of soot formation for the reference flames, confirming the validity of the employed soot modeling techniques as well as of the kinetic scheme EST3 introduced in the present study.

6. Results and discussion

The previous section has shown that both DSM and S-EQMOM modeling approaches tend to perform similarly for the KAUST flames [11] using the new reaction mechanism EST3, specifically designed to use

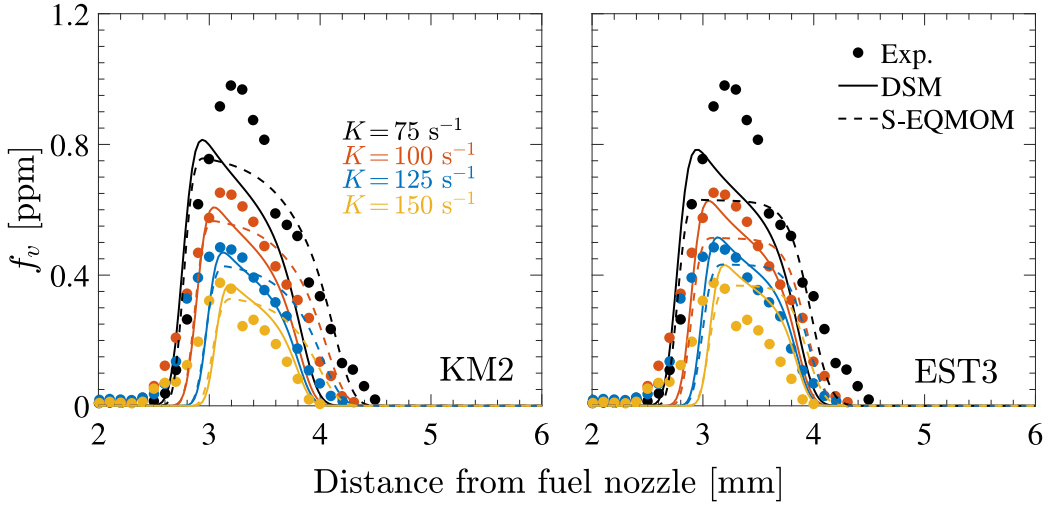

Fig. 4. Comparison between the numerical (curves) and experimental (symbols) profiles for soot volume fraction (f_v) with DSM (solid) and S-EQMOM (dashed) models for KM2 [22] (left) and EST3 (right) kinetic schemes. Experimental data are from Wang and Chung [11].

pyrene as lumped PAH species for particle nucleation. Therefore, these modeling strategies are adopted to investigate the new set of counter-flow diffusion flames measured at Karlsruhe Institute of Technology (KIT) [23]. The predictive capabilities of these modeling approaches are evaluated for strain rate sensitivity and dilution effects of soot formation by comparing the computed results against the measured soot volume fraction profiles and particle size distribution data. To the best of our knowledge, this is the first time such a comparison has been made on the same datasets. Additionally, the sub-processes of the soot formation are analyzed based on both modeling strategies. The flames under investigation are listed in Table 1.

6.1. Evaluation of soot volume fraction profiles

The measured (symbols) and computed (curves) profiles of soot volume fraction f_v are compared in Fig. 5 for strain rates 50 s^{-1}, 60 s^{-1}, and 70 s^{-1} at a constant fuel mass fraction of $Y_{F,f} = 0.30$. Both soot models predict the qualitative trend of the reduced f_v with increasing strain rate. The measured flames exhibit soot formation type counterflow flames, where soot particles, incepted on the fuel-rich side of the flame, are convected towards the stagnation plane. Compared to DSM, higher f_v values are obtained with the S-EQMOM model. However, the width of the sooting zone is well predicted with the S-EQMOM model compared to DSM. A detailed analysis of different soot formation sub-processes will be presented later to investigate the differences in the modeling results for the two retained methodologies. While quantitative f_v predictions are maintained within the same order of magnitude in simulations, both models predict a lower sensitivity of f_v to strain rate compared to the experiments.

The modeled soot volume fraction profiles for varying levels of fuel mass fraction $Y_{F,f}$ at a constant strain rate of $K = 60$ s^{-1} are compared in Fig. 6 against measured SMPS data. An increase in f_v for higher ethylene concentration is obtained experimentally as well as in the modeling results. For the $Y_{F,f} = 0.35$, the S-EQMOM slightly overpredicts the soot formation, while the DSM model matches the measuring results fairly well. However, the reduction of soot formation with reduced ethylene mass fractions is stronger in the measurements as compared to the computed results for both models. Apparently, the soot formation is highly sensitive to the ethylene content in the fuel as 5% of decrement in ethylene mass fraction from $Y_{F,f} = 0.35$ leads to approximately 71% reduction in f_v measured at HAB = 5.5 mm. In the DSM model, such a drop in f_v values is obtained at 15% of reduction in $Y_{F,f} = 0.35$. Comparing the soot models, the S-EQMOM predicts higher amounts of soot volume fraction than the DSM model

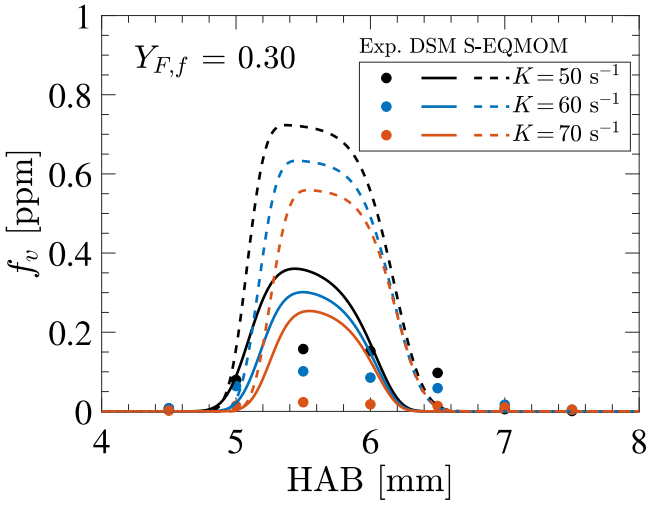

Fig. 5. Comparison between the numerical (curves) and experimental (symbols) soot volume fraction profiles for varying strain rates at a fuel mass fraction of $Y_f = 0.30$.

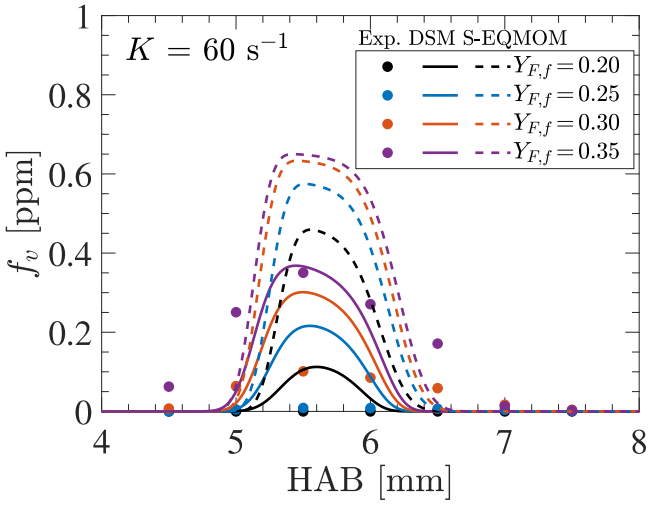

Fig. 6. Comparison between the numerical (curves) and experimental (symbols) soot volume fraction profiles for varying fuel mass fraction at a strain rate of $K = 60$ s^{-1}.

in all investigated flame configurations. While the position of the peak value and particle stagnation plane agree well, the position of the soot formation zone in the S-EQMOM is displaced to higher HAB positions. Overall, the results are reasonably close to the experimental data taking into account the large uncertainties associated with the predictions of larger PAH concentrations in the EST3 mechanism.

The discrepancy between experimental data and modeling results in counterflow diffusion flames is a common observation in the literature across various modeling approaches [12,13,45,49,50]. These deviations are particularly observed near the stagnation plane. One possible reason for this discrepancy is the variation in the prediction of the flame stagnation position by the models, as measurements for velocity were not conducted and no scaling or numerical shift of the profiles was applied. In cases where the conditions of the studied flames align closely with those of other publications, a better agreement between the soot formation zones is observed, as is the case in the current study. The absolute misalignment between experimental data and models roughly scales with the distance between the fuel and oxidizer ducts, which in the current study is relatively large. The observed diffusion of soot in fuel-rich regions may also be attributed to experimental limitations. However, the exact cause of this systematic misalignment in some flames remains unclear, and further investigation is needed to determine its source.

Additionally, it is important to note, that the soot models were not specifically tuned for the investigated flames. For highly sooting conditions ($Y_{F,f} = 1$ as in KAUST flames), the predictive accuracy of both soot models is reasonably good, though, a stronger variability on the two soot models is observed for these challenging conditions with high fuel dilution and low soot formation. This is because, in flames with high fuel dilution that exhibit low-sooting conditions, the soot formation process is primarily limited by the initial inception step. While the bi-directional coupling between the gas-phase and soot model has a significant effect on the pyrene concentration profile in the gas phase (due to its very low concentration), the concentration of C_2H_2 (a primary contributor for HACA) is not significantly affected due to its overall high value. The sensitivity of the inception process to the gas phase conditions often makes it challenging to accurately capture the initial step and subsequent soot formation process.

6.2. Analyses of the soot sub-processes

To better understand the predictive capabilities of soot models an analysis of the different sub-processes is conducted. The contribution to the soot growth by nucleation, condensation, and HACA surface growth are compared in Fig. 7 for varying strain rates at a constant fuel mass fraction of $Y_{F,f} = 0.30$. Both modeling results show a decreasing peak value for the nucleation, condensation, and surface growth rates for increasing strain rates. The DSM and S-EQMOM models agree on the overall trends and also on the shape of the soot formation rate profiles. While the soot volume fraction profiles in Fig. 5 contain a significant sensitivity for strain rate variations, only small differences in the underlying soot production rates can be observed. The computed rate profiles for different sub-processes mainly differ in the peak position and quantitative values. The condensation and, in the case of the S-EQMOM method, also the nucleation process is markedly influenced by strain rate variations while the difference in the surface growth reactions is almost negligible. Comparing the nucleation rates between the models, it can be seen, that only minor differences are present at the start of the soot formation at HAB = 7 mm up to approximately HAB = 6.2 mm since the nucleation process is solely depending on the underlying gas-phase and on the amount of the PAH species pyrene that initiates the inception step within both soot models. The condensation and surface growth processes on the other hand depend additionally on the modeled PSD, leading to larger deviations between both models. Due to the bi-directional coupling between the gas phase and the particle model, small deviations in some of these processes are also

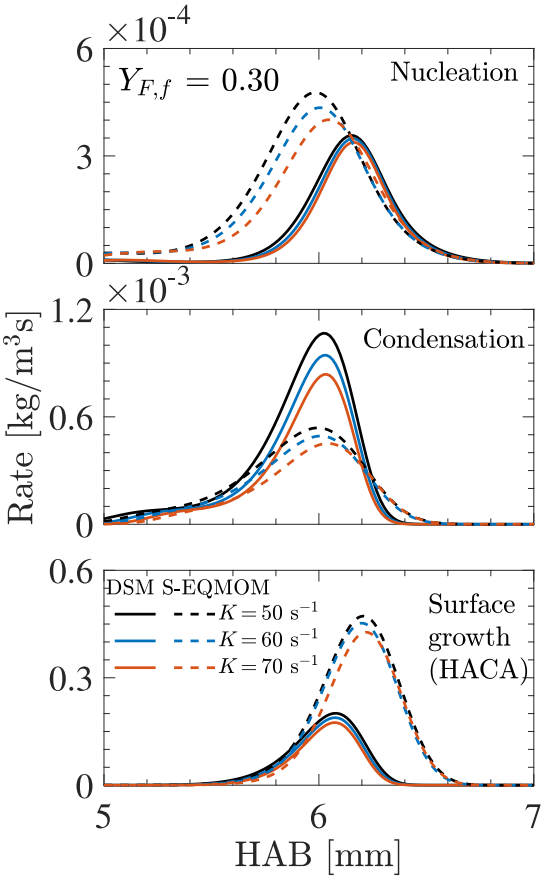

Fig. 7. Computed profiles of soot growth sub-processes with the DSM (solid) and S-EQMOM soot model (dashed) for varying strain rates (indicated by color) at a fuel mass fraction of $Y_f = 0.30$.

altering the underlying gas-phase composition. In fact, the nucleation and condensation processes reduce the pyrene concentration in the gas phase. Hence, larger deviations in nucleation can be observed at lower HAB positions, when condensation and surface growth processes are dominantly affecting the gas-phase chemistry. Fig. 2 demonstrates that the acetylene profile (which impacts the surface growth) is primarily influenced by fuel dilution and only slightly decreases for higher strain rates. However, increased strain rates significantly reduce the residence time of particles in the flame due to higher gas phase velocities. Consequently, despite similar surface growth rates, the variation in residence times leads to different soot volume fractions. Considering relatively small variations in the soot formation rates, the difference in the amount of soot formed for different strain rates can be mainly attributed to varying flow velocities and subsequently the change in the residence times of soot particles.

The rate profiles of different soot sub-processes for varying fuel mass fractions at a constant strain rate of $K = 60\,s^{-1}$ are shown in Fig. 8. The rates for all the sub-processes are significantly increased at higher fuel mass fractions in the fuel stream at a constant strain rate (and thus similar residence times). The increase in soot volume fractions at increasing ethylene content in fuel, as observed in Fig. 6, can therefore be mainly ascribed to the increment in soot formation rates through HACA surface reactions, and higher concentration of soot precursors (not shown) affecting soot inception rates. Again, both DSM and S-EQMOM models follow similar trends and agree in the overall shape; however, quantitative deviations and a shift of the profiles can be observed. In both studies, Figs. 7 and 8, the DSM model leads on one hand to higher condensation rates than the S-EQMOM model, while on the other hand, nucleation rates are reduced which can be

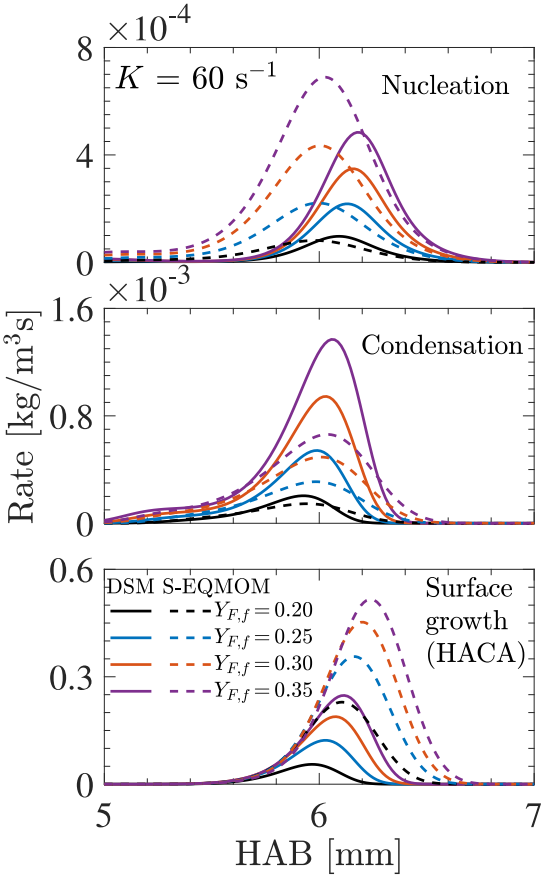

Fig. 8. Computed profiles of soot growth sub-processes with the DSM (solid) and S-EQMOM soot model (dashed) for varying fuel mass fraction (indicated by color) at a strain rate of $K = 60\,s^{-1}$.

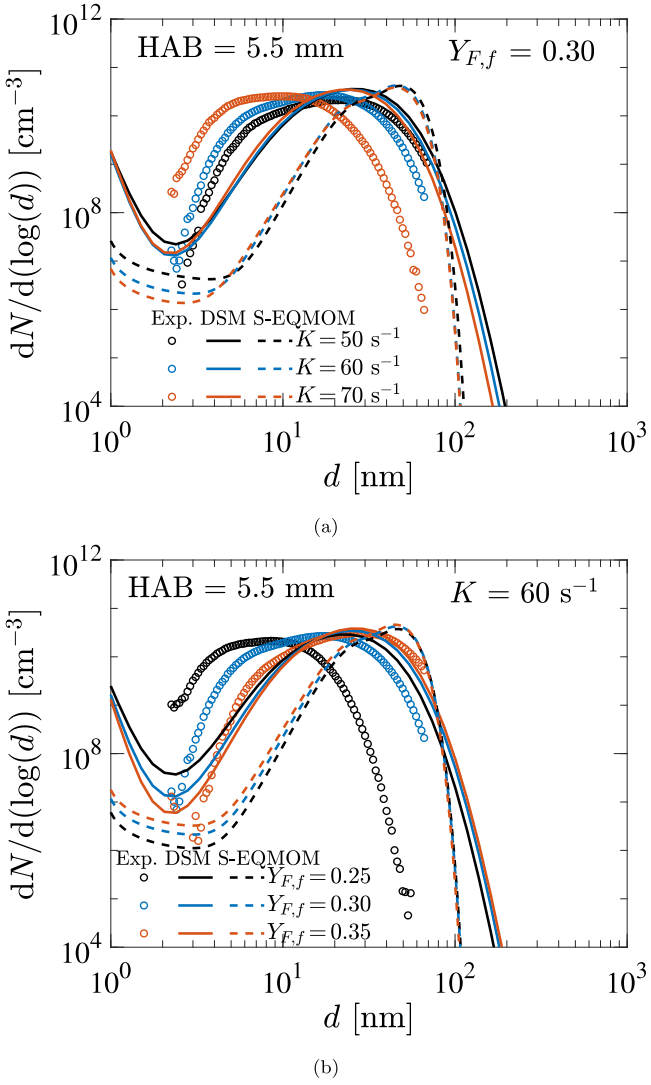

Fig. 9. Comparison between the numerical (curves) and experimental (symbols) PSD for varying strain rates at a fuel mass fraction of $Y_{F,f} = 0.30$ (a), and for varying fuel mass fraction at a strain rate of $K = 60\,s^{-1}$ (b).

explained by the dependence of both processes on the amount of pyrene. These results clearly highlight the competing processes. The S-EQMOM exhibits higher HACA surface growth rates leading also to higher soot volume fractions due to surface growth, which is the largest contributor to soot formation.

Overall, the surface growth mechanism through the HACA pathway contributes significantly to the overall soot loading in terms of soot volume or mass, surpassing the contribution of the inception process or PAH deposition onto the particle surface by several orders of magnitude (as identified in earlier works [11,49] for flames at atmospheric pressure). This is attributed to the large differences in concentration between the C_2H_2 and PAH species, which play key roles in the respective soot processes. However, it is important to note that surface growth is not the sole factor influencing the final soot profile. Other factors, such as residence time due to varying strain rates, the profile and peak concentration of gas-phase precursors, and the position of the flame relative to the stagnation plane, also strongly influence soot formation in the investigated counterflow configurations.

6.3. Evaluation of particle size distributions

In addition to the volume fraction, particle size distributions (PSD) were measured for the investigated flames. The experimental and modeling results of PSDs at a height above the burner of HAB = 5.5 mm (location of highest f_v value in the measurements) are compared in Fig. 9. The experimental SMPS measurement range is limited to particles with a mobility diameter (d_m) between $2\,nm \leqslant d_m \leqslant 79\,nm$, and consists mainly of the log-normal mode of PSD referring to larger particles, while the inception mode is only partially visible at the smallest detectable diameters. Furthermore, it should be noted that there is a significant loss of particles smaller than 10 nm in the probe, tubes, and mobility sizer, resulting in increased experimental uncertainties for the small particle sizes [23]. PSD profiles for a constant fuel mass fraction of $Y_{F,f} = 0.30$ with varying strain rates are displayed in Fig. 9(a), whereas in Fig. 9(b), results for varying fuel mass fractions at a constant strain rate of $K = 60\,s^{-1}$ are presented.

The current soot modeling approaches are based on the volume equivalent particle diameter d_p, whereas measurement data represent mobility sizes (d_m) of particles. A scaling is applied to convert d_m to d_p as proposed in the Refs. [51,52]. Since the current modeling approach assumes the spherical nature of soot particles, the conversion of particle sizes using empirical scaling may be ambiguous, considering the limitations of the empirical Cunningham slip correction transformation, uncertainty of the number of primary particles per aggregate when converting mobility sizes (d_m) to spherical particle sizes (d_p). To address these considerations and avoid ambiguity, the particle diameter in Fig. 9 is generalized with the symbol d and should be interpreted as d_m for measurements and d_p for simulations.

As evident in Fig. 9(a), the median diameter of the log-normal mode shifts to larger particle diameters for decreasing strain rates at constant

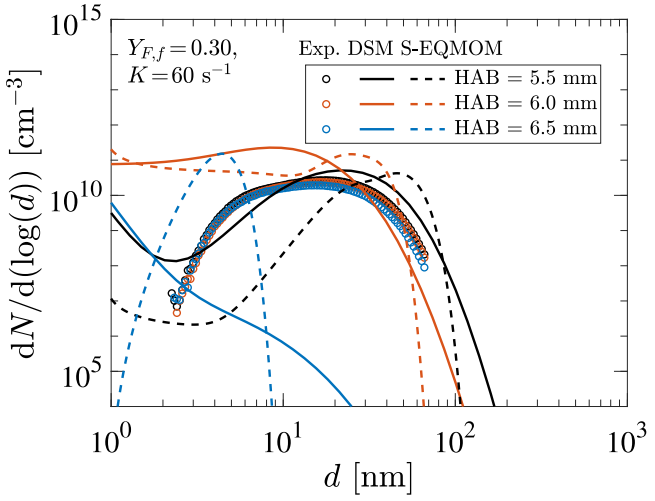

Fig. 10. Comparison between the numerical (curves) and experimental (symbols) PSD profiles at different HAB positions (indicated by color) for the flame with $Y_{F,f} = 0.30$ and $K = 60\,s^{-1}$.

fuel mass fraction. A similar shift towards larger diameters is also noticed in PSDs for higher ethylene mass fractions at constant strain rates (see Fig. 9(b)). However, the number density at this peak position of PSD is not significantly affected by a strain rate or fuel mass fraction variation. Only a slight reduction in number density is observed with a decrement in strain rate or ethylene content in the fuel. The computed profiles by DSM and S-EQMOM strategies favorably capture the shape of PSD for varied strain rates and fuel compositions. The stronger shift in the PSD profiles can be observed in the measurements as a consequence of the high sensitivity of soot volume fraction to strain rate and fuel composition variations for the investigated flames. The simulated profiles, on the other hand, show only a marginal shift in the median diameter of PSD as the soot sensitivity is under-predicted in the simulations.

The modeling results are dominated by the log-normal mode as well indicating that the soot inception area is placed at a higher HAB. The particle evolution is mainly influenced by particle growth and coagulation events during its convection to the particle stagnation plane at smaller HAB. The shape of the DSM results matches the experimentally observed profile quite closely, also the qualitative trends in PSD shift are captured well by the DSM model. The S-EQMOM profiles are dominated by a peak at a diameter of 50 nm in Fig. 9(a). Here, the superposition of the three underlying sub-KDFs represented by gamma functions results in a distinct peak of the second mode. The position of the peak is equivalent to the position of one of the sub-KDFs containing the largest particles, while the remaining two sub-KDFs represent the first mode and particles in between. Overall, the modeling results are consistent with experimental findings regarding the marginal change in the number density of the peak of the log-normal mode. However, the peak position of this mode is only slightly shifted for varying strain rates and fuel mass fractions in computations.

A more detailed comparison of PSD evolution is presented in Fig. 10, where PSD profiles at different HABs are shown for the flame at $Y_{F,f} = 0.30$ and $K = 60\,s^{-1}$. The computed PSD profiles show strong variations in PSD shape along the HAB, including a transition from unimodal to a bimodal distribution. However, measured PSD profiles hardly show this transition, and PSDs predominantly exhibit the log-normal distribution. As it occurs in SF-type flame, consistent soot inception occurs at higher HABs (oxidizer side of stagnation plane), giving unimodal PSD shape (HAB = 6.0 mm) in simulations. At the spatial position of HAB = 6.5 mm, which marks the start of the soot formation process, differences between the PSD shape predictions by the S-EQMOM and DSM models are prominent. The S-EQMOM model shows a slight contribution of surface growth, indicating that particles have already undergone some level of growth by this point. In contrast, the DSM model does not show significant surface growth at the start of the soot formation process (as can be seen also Figs. 7 and 8). This slight disparity in spatial positions of soot growth rate profiles essentially leads to a different shape of the particle size distribution (PSD) by both models at this position. Soot particles grow by surface growth and coagulation while being convicted towards the stagnation plane. In such conditions, the PSD becomes bimodal, with an increase in the median diameter of the log-normal mode.

Soot inception predominantly occurs for both models at HABs greater than 5.5 mm, with the peak of inception at approximately HAB = 6 mm and HAB = 6.25 mm for the respective models. However, at HAB = 5.5 mm, coagulation dominates the soot evolution processes. In Fig. 10 it is evident that smaller particles of the first mode, which are present at HAB = 6 mm in both models, undergo rapid growth and coagulation, transitioning towards the second mode. Due to slight variations in the spatial rate profiles of sooting subprocesses between the models, the coagulation process is more advanced in the S-EQMOM model at HAB = 5.5 mm, resulting in fewer inception particles despite higher inception rates in Figs. 8 and 7. The evolution of the growth processes seems to overweigh the inception rate at this position in the flame. This PSD evolution is qualitatively well captured by both DSM and S-EQMOM models. However, the soot formation is found to start at higher HABs in experiments, as evident from f_v profiles (see Fig. 5). Therefore discrepancy between numerical and measured profiles of PSD suggests that the soot inception locations are predicted at lower HABs in simulations as compared to measurements.

7. Concluding remarks

A systematic investigation of soot formation and particle size distributions in laminar ethylene counterflow flames is conducted by combining experimental and numerical methodology. The focus is given to the analysis of the influence of strain rate and fuel dilution on sooting characteristics. Such investigation is reported for the first time to the best of the authors' knowledge.

The modeling strategy consists of a recently developed reaction mechanism considering the description of PAHs up to A4 and two detailed soot modeling approaches DSM and S-EQMOM. The modeling results are compared against dedicated experiments with optical diagnostics measuring the soot volume fraction profiles and the PSD for a wide range of operation conditions. First, the kinetic scheme EST3 is validated for the prediction of gas-phase species including PAHs and temperature showing excellent agreement. The soot modeling results also closely reproduce their experimental counterparts regarding the strain rate and dilution effects on the soot volume fraction profiles. Additionally, the results suggest that strain rate variations mainly influence the residence time while only slightly affecting the rates of the underlying soot production processes. Furthermore, a reduction in the ethylene content of the fuel strongly reduces the soot production rates and, thus, the overall soot volume fraction. Modeled PAH-based sub-processes, namely inception, and condensation, exhibit higher sensitivity to the strain and fuel variations than the HACA process. The experimental results show a high sensitivity of soot formation to the ethylene content compared to numerical results. Overall, the simulation results are in close agreement with the experimental data revealing certain over-predictions acceptable for the soot models. Still, the predictivity of the models is considered good in the context of soot investigations for this wide range of flame conditions.

Both models show similar quantitative trends under strain rate and fuel composition variation, suggesting a high generality of the findings and being independent of the applied soot modeling strategy. Differences between DSM and S-EQMOM are limited to minor deviations of the overall quantity in the rate profiles of different sub-processes

or slight shifts in their peak positions. One of the key highlights of this study is the joint experimental and numerical investigation of the soot PSDs for varying strain rates and fuel compositions, where a close agreement is observed between modeling and measurement for the response of soot PSD to these two changes. Nevertheless, the numerical PSD profiles exhibit reduced sensitivities to these variations as compared to the measurements.

Additionally, the present study demonstrates the promising capabilities of the kinetic scheme EST3 in combination with detailed soot models in capturing experimentally observed responses of soot formation and PSD evolution in laminar flames. While this study focuses on the well-understood ethylene fuel, the applied kinetic mechanism allows an extension of these investigations to more complex fuels such as kerosene surrogates.

Declaration of competing interest

The authors declare that they have no known competing financial interests or personal relationships that could have appeared to influence the work reported in this paper.

Acknowledgments

The research leading to these results has received funding from the European Union's Horizon 2020 Programme under the ESTiMatE project, grant agreement No. 821418.

References

[1] C. Voigt, J. Kleine, D. Sauer, R.H. Moore, T. Bräuer, P. Le Clercq, S. Kaufmann, M. Scheibe, T. Jurkat-Witschas, M. Aigner, et al., Cleaner burning aviation fuels can reduce contrail cloudiness, Commun. Earth Environ. 2 (1) (2021) 114.

[2] European Commission and Directorate-General for Mobility and Transport and Directorate-General for Research and Innovation, Flightpath 2050: Europe's Vision for Aviation: Maintaining Global Leadership and Serving Society's Needs, Publications Office of the European Union, Luxembourg, Luxembourg, 2011.

[3] M. Sirignano, J. Kent, A. D'Anna, Modeling formation and oxidation of soot in nonpremixed flames, Energy Fuels 27 (4) (2013) 2303–2315.

[4] M. Sirignano, J. Kent, A. D'Anna, Further experimental and modelling evidences of soot fragmentation in flames, Proc. Combust. Inst. 35 (2) (2015) 1779–1786.

[5] A. Cuoci, A. Frassoldati, T. Faravelli, E. Ranzi, Soot formation in unsteady counterflow diffusion flames, Proc. Combust. Inst. 32 I (1) (2009) 1335–1342.

[6] P. Rodrigues, B. Franzelli, R. Vicquelin, O. Gicquel, N. Darabiha, Unsteady dynamics of PAH and soot particles in laminar counterflow diffusion flames, Proc. Combust. Inst. 36 (1) (2017) 927–934.

[7] W. Pejpichestakul, A. Frassoldati, A. Parente, T. Faravelli, Soot modeling of ethylene counterflow diffusion flames, Combust. Sci. Technol. (2018).

[8] H. Wang, D. Du, C. Sung, C. Law, Experiments and numerical simulation on soot formation in opposed-jet ethylene diffusion flames, Symp. (Int.) Combust. 26 (2) (1996) 2359–2368.

[9] H. Böhm, K. Kohse-Höinghaus, F. Lacas, C. Rolon, N. Darabiha, S. Candel, On PAH formation in strained counterflow diffusion flames, Combust. Flame 124 (1–2) (2001) 127–136.

[10] M. Yamamoto, S. Duan, S. Senkan, The effect of strain rate on polycyclic aromatic hydrocarbon (PAH) formation in acetylene diffusion flames, Combust. Flame 151 (3) (2007) 532–541.

[11] Y. Wang, S. Chung, Strain rate effect on sooting characteristics in laminar counterflow diffusion flames, Combust. Flame 165 (2016) 433–444.

[12] S. Kruse, A. Wick, P. Medwell, A. Attili, J. Beeckmann, H. Pitsch, Experimental and numerical study of soot formation in counterflow diffusion flames of gasoline surrogate components, Combust. Flame 210 (2019) 159–171.

[13] E. Quadarella, J. Guo, H.G. Im, A consistent soot nucleation model for improved prediction of strain rate sensitivity in ethylene/air counterflow flames, Aerosol Sci. Technol. 56 (7) (2022) 636–654.

[14] P.H. Joo, Y. Wang, A. Raj, S.H. Chung, Sooting limit in counterflow diffusion flames of ethylene/propane fuels and implication to threshold soot index, Proc. Combust. Inst. 34 (1) (2013) 1803–1809.

[15] F. Carbone, F. Cattaneo, A. Gomez, Structure of incipiently sooting partially premixed ethylene counterflow flames, Combust. Flame 162 (11) (2015) 4138–4148.

[16] K. Gleason, F. Carbone, A. Gomez, Effect of temperature on soot inception in highly controlled counterflow ethylene diffusion flames, Combust. Flame 192 (2018) 283–294.

[17] Y. Wang, S.H. Chung, Soot formation in laminar counterflow flames, Prog. Energy Combust. Sci. 74 (2019) 152–238.

[18] F.P. Hagen, P. Vlavakis, H. Bockhorn, R. Suntz, D. Trimis, From molecular to sub-μm scale: The interplay of precursor concentrations, primary particle size, and carbon nanostructure during soot formation in counter-flow diffusion flames, Combust. Flame (2023) 112729.

[19] C. Hoerlle, F. Pereira, Effects of CO_2 addition on soot formation of ethylene non-premixed flames under oxygen enriched atmospheres, Combust. Flame 203 (2019) 407–423.

[20] S. Salenbauch, C. Hasse, M. Vanni, D.L. Marchisio, A numerically robust method of moments with number density function reconstruction and its application to soot formation, growth and oxidation, J. Aerosol Sci. 128 (2019) 34–49.

[21] A. Ramirez Hernandez, T. Kathrotia, T. Methling, M. Braun-Unkhoff, U. Riedel, Reaction model development of selected aromatics as relevant molecules of a kerosene surrogate—The importance of m-xylene within the combustion of 1,3,5-trimethylbenzene, J. Eng. Gas Turbines Power 144 (2) (2022) 021002.

[22] Y. Wang, A. Raj, S.H. Chung, A PAH growth mechanism and synergistic effect on PAH formation in counterflow diffusion flames, Combust. Flame 160 (9) (2013) 1667–1676.

[23] F.P. Hagen, P. Vlavakis, M. Seitz, T. Klövekorn, H. Bockhorn, R. Suntz, D. Trimis, Soot nanoparticle sizing in counterflow flames using in-situ particle sampling and differential mobility analysis verified with two-colour time-resolved laser-induced incandescence, Proc. Combust. Inst. 39 (2023) 1119–1128.

[24] A.M. Valencia-López, F. Bustamante, A. Loukou, B. Stelzner, D. Trimis, M. Frenklach, N.A. Slavinskaya, Effect of benzene doping on soot precursors formation in non-premixed flames of producer gas (PG), Combust. Flame 207 (2019) 265–280.

[25] R. Khare, P. Vlavakis, T. Von Langenthal, A. Loukou, M. Khosravi, U. Kramer, D. Trimis, Experimental investigation of the effect of hydrogen addition on the sooting limit and structure of methane/air laminar counterflow diffusion flames, Fuel 324 (2022) 124506.

[26] C.R. Shaddix, Correcting thermocouple measurements for radiation loss: a critical review, 1999.

[27] M. Sentko, S. Schulz, C. Weis, B. Stelzner, C. Anderlohr, M. Vicari, D. Trimis, Experimental investigation of synthesis gas production in fuel-rich oxy-fuel methane flames, Fuel 317 (2022) 123452.

[28] Y. Karakaya, J. Sellmann, I. Wlokas, T. Kasper, Influence of the sampling probe on flame temperature, species, residence times and on the interpretation of ion signals of methane/oxygen flames in molecular beam mass spectrometry measurements, Combust. Flame 229 (2021) 111388.

[29] H. Shariatmadar, P.G. Aleiferis, R. Lindstedt, Particle size distributions in turbulent premixed ethylene flames crossing the soot inception limit, Combust. Flame 243 (2022) 111978.

[30] F.P. Hagen, A. Rinkenburger, J. Günther, H. Bockhorn, R. Niessner, R. Suntz, A. Loukou, D. Trimis, C. Haisch, Spark discharge-generated soot: Varying nanostructure and reactivity against oxidation with molecular oxygen by synthesis conditions, J. Aerosol Sci. 143 (2020) 105530.

[31] I. Frenzel, H. Krause, D. Trimis, Study on the influence of ethanol and butanol addition on soot formation in iso-octane flames, Energy Procedia 120 (2017) 721–728.

[32] A. Ramirez Hernandez, T. Kathrotia, T. Methling, M. Braun-Unkhoff, U. Riedel, An upgraded chemical kinetic mechanism for iso-octane oxidation: Prediction of polyaromatics formation in laminar counterflow diffusion flames, J. Eng. Gas Turbines Power 145 (6) (2023) 061006.

[33] T. Kathrotia, P. Oßwald, C. Naumann, S. Richter, M. Köhler, Combustion kinetics of alternative jet fuels, Part-II: Reaction model for fuel surrogate, Fuel 302 (2021) 120736.

[34] T. Kathrotia, T. Methling, https://www.dlr.de/vt/mechanisms, 2022.

[35] D.G. Goodwin, H.K. Moffat, R.L. Speth, Cantera: An object-oriented software toolkit for chemical kinetics, thermodynamics, and transport processes, 2022.

[36] S. Friendlander, Smoke, Dust and Haze: Fundamentals of Aerosol Dynamics, Oxford University Press, New York, USA, 2000.

[37] M. Frenklach, H. Wang, Detailed modeling of soot particle nucleation and growth, Symp. (Int.) Combust. 23 (1) (1991) 1559–1566.

[38] J. Appel, H. Bockhorn, M. Frenklach, Kinetic modeling of soot formation with detailed chemistry and physics: laminar premixed flames of C2 hydrocarbons, Combust. Flame 121 (1–2) (2000) 122–136.

[39] S. Kumar, D. Ramkrishna, On the solution of population balance equations by discretization–I. a fixed pivot technique, Chem. Eng. Sci. 51 (8) (1996) 1311–1332.

[40] A. Kalbhor, J. van Oijen, Effects of hydrogen enrichment and water vapour dilution on soot formation in laminar ethylene counterflow flames, Int. J. Hydrogen Energy 45 (43) (2020) 23653–23673.

[41] A. Kalbhor, Model Development and Numerical Investigation of Soot Formation in Combustion (Ph.D. thesis), Eindhoven University of Technology, the Netherlands, 2023.

[42] C. Yuan, F. Laurent, R.O. Fox, An extended quadrature method of moments for population balance equations, J. Aerosol Sci. 51 (2012) 1–23.

[43] S. Salenbauch, Modeling of Soot Formation and Oxidation in Reacting Flows (Ph.D. thesis), Technical University of Darmstadt, 2018.

[44] F. Ferraro, S. Gierth, S. Salenbauch, W. Han, C. Hasse, Soot particle size distribution reconstruction in a turbulent sooting flame with the split-based extended method of moments, Phys. Fluids 075121 (2022).
[45] Y. Wang, W. Han, T. Zirwes, A. Attili, L. Cai, H. Bockhorn, L. Yang, Z. Chen, A systematic analysis of chemical mechanisms for ethylene oxidation and PAH formation, Combust. Flame 253 (2023) 112784.
[46] B. Somers, The Simulation of Flat Flames with Detailed and Reduced Chemical Models (Ph.D. thesis), Eindhoven University of Technology, 1994.
[47] CHEM1D: One-Dimensional Laminar Flame Code, Eindhoven University of Technology, 2022.
[48] A. Zschutschke, D. Messig, A. Scholtissek, C. Hasse, Universal laminar flame solver (ULF), 2017.
[49] L. Xu, F. Yan, M. Zhou, Y. Wang, S.H. Chung, Experimental and soot modeling studies of ethylene counterflow diffusion flames: Non-monotonic influence of the oxidizer composition on soot formation, Combust. Flame 197 (2018) 304–318.
[50] K.C. Kalvakala, V.R. Katta, S.K. Aggarwal, Effects of oxygen-enrichment and fuel unsaturation on soot and NO emissions in ethylene, propane, and propene flames, Combust. Flame 187 (2018) 217–229.
[51] J. Singh, R.I. Patterson, M. Kraft, H. Wang, Numerical simulation and sensitivity analysis of detailed soot particle size distribution in laminar premixed ethylene flames, Combust. Flame 145 (1–2) (2006) 117–127.
[52] A.D. Abid, J. Camacho, D.A. Sheen, H. Wang, Quantitative measurement of soot particle size distribution in premixed flames–the burner-stabilized stagnation flame approach, Combust. Flame 156 (10) (2009) 1862–1870.